

Design and implementation of dynamic near-infrared optical tomographic imaging instrumentation for simultaneous dual-breast measurements

Christoph H. Schmitz, David P. Klemer, Rosemarie Hardin, Michael S. Katz, Yaling Pei, Harry L. Graber, Mikhail B. Levin, Rita D. Levina, Nelson A. Franco, William B. Solomon, and Randall L. Barbour

Dynamic near-infrared optical tomographic measurement instrumentation capable of simultaneous bilateral breast imaging, having a capability of four source wavelengths and 32 source–detector fibers for each breast, is described. The system records dynamic optical data simultaneously from both breasts, while verifying proper optical fiber contact with the tissue through implementation of automatic schemes for evaluating data integrity. Factors influencing system complexity and performance are discussed, and experimental measurements are provided to demonstrate the repeatability of the instrumentation. Considerations in experimental design are presented, as well as techniques for avoiding undesirable measurement artifacts, given the high sensitivity and dynamic range ($1:10^9$) of the system. We present exemplary clinical results comparing the measured physiologic response of a healthy individual and of a subject with breast cancer to a Valsalva maneuver. © 2005 Optical Society of America

OCIS codes: 170.6960, 170.3830, 170.1610.

1. Introduction

The past several years have witnessed significant advances in systems designed for biomedical applications of near-infrared spectroscopy and tomographic image reconstruction. Time-division-multiplexed near-infrared systems capable of studying physio-

logic responses within human tissue have increased in performance and complexity.^{1–4} Production imagers used for tomographic image reconstruction are currently available having four-wavelength capability and up to 8192 source–detector data channels.¹

In this paper, we discuss the design and implementation of a near-infrared imager used for physiology and pathophysiology studies that is based on simultaneous, bilateral near-infrared breast measurements. The system described herein uses a time-division-multiplexed scheme with a spatially combined optical source comprising up to four near-infrared wavelengths. The same basic system architecture has been used in imagers designed for a variety of biomedical applications, including functional neuroimaging, small-animal imaging, evaluation of breast pathologies, and evaluation of the reactivity of the peripheral vasculature in limbs.^{5–8}

System complexity is proportional to the number of data channels, defined as

$$\text{number of data channels} = \text{WL} \times \text{S} \times \text{D}, \quad (1)$$

where WL represents the number of distinct near-

C. H. Schmitz (christoph.schmitz@downstate.edu), Y. Pei, H. L. Graber, M. B. Levin, R. D. Levina, and R. L. Barbour are with NIRx Technologies, LLC., 15 Cherry Lane, Glen Head, New York 11545. C. H. Schmitz, R. Hardin, M. S. Katz, H. L. Graber, M. B. Levin, N. A. Franco, W. B. Solomon, and R. L. Barbour were with the Downstate Medical Center, State University of New York, Box 25, 450 Clarkson Avenue, Brooklyn, New York 11203-1298. R. Hardin, N. Franco, and M. Katz are with the New York State Department of Health Empire Clinical Research Investigator Program (ECRIP) fellows at Kings County Hospital Center, 451 Clarkson Avenue, Brooklyn, New York 11203. D. P. Klemer is now with the Department of Electrical Engineering and Computer Science, University of Wisconsin–Milwaukee, P.O. Box 784, Milwaukee, Wisconsin 53201.

Received 21 July 2004; revised manuscript received 11 November 2004; accepted 17 November 2004.

0003-6935/05/112140-14\$15.00/0

© 2005 Optical Society of America

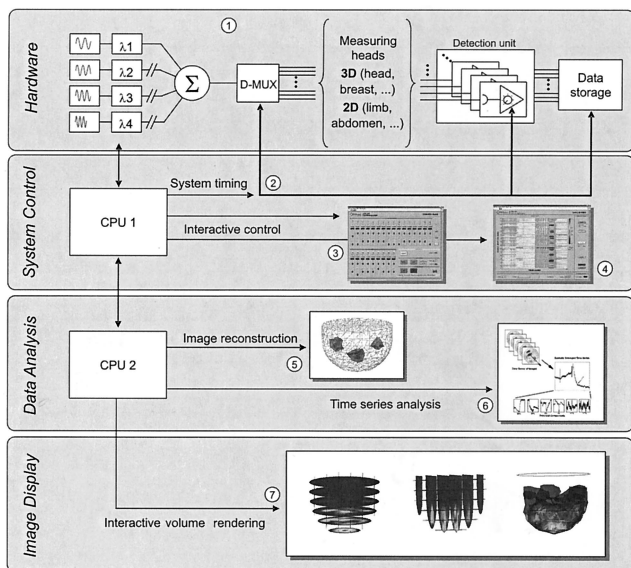


Fig. 1. Block diagram of DYNOT system hardware and software components, depicting seven levels of system integration: 1, hardware; 2, data acquisition and timing; 3, instrument control and diagnosis software; 4, real-time data display; 5, image-reconstruction software; 6, data-image time-series analysis; 7, interactive volume rendering.

infrared source wavelengths (e.g., WL = 2–760 and 830 nm—in the design described in this paper), S represents the number of source illumination fibers, and D represents the number of detector fibers in the measuring head. As the number of data channels increases, automated setup and error-checking software become essential. Long-duration studies in which data are collected over an extended baseline period (in order to examine slowly changing physiologic behavior) place significant acceptability constraints on system long-term stability and drift.

Here we describe the implementation of a dual-head imaging system for simultaneous bilateral measurements of the human breast. Simultaneous recording of dynamic measurements from both breasts allows for implementation of novel signal-processing algorithms and evaluation of dynamic details of physiology that were heretofore unavailable, such as left-versus-right differences in delay times and phase shifts in periodic physiologic phenomena.

2. Dynamic Near-Infrared Optical Tomographic Architecture and Functionality

A multichannel dynamic near-infrared optical tomographic (DYNOT) imaging system comprises seven layers of hardware and software integration, as depicted in the block diagram of Fig. 1.

A. Hardware

Optical energy from up to four laser diode illumination sources (1) is intensity modulated at a unique frequency (3–10 kHz) for each source, for subsequent lock-in detection. Energy from the sources is spatially combined and coupled into an electromechanical op-

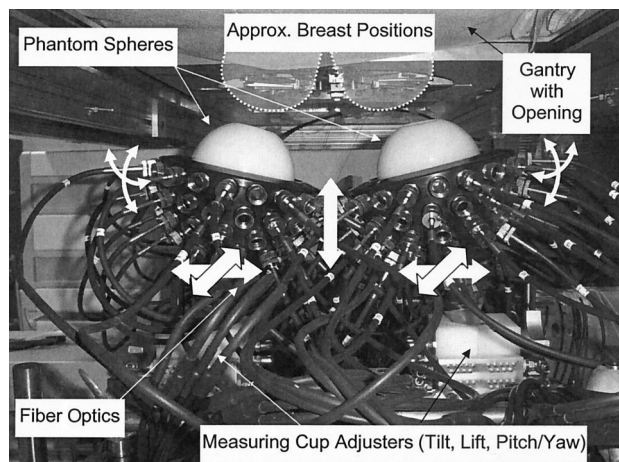


Fig. 2. Photograph of measuring head used for simultaneous dual-breast measurements. Thirty-one source-detector fibers are distributed over the surface of each breast.

tical switch (demultiplexer, D-MUX) that employs a rotating mirror to sequentially redirect the light into the illumination fibers at a 75-Hz switching rate; this device has been described in detail in Ref. 2. The dual-breast imager employs a novel, modified optical switch design with a rotating stack of two parallel mirrors, the top one being semitransparent (reflectivity $R \cong 50\%$) for both wavelengths, while the bottom one is highly reflective ($R > 98\%$) for both wavelengths. The purpose of this assembly is to split the laser beam and to redirect half of its power into each of two groups of illumination fibers. Each group, consisting of up to 32 fibers, illuminates one breast. Therefore, the optical switch used in the dual-breast imager accomplishes parallel dual 32-fiber time-multiplexing, rather than true 64-channel switching. This approach has the advantage of doubling the number of available illumination points without loss of scan speed and with only moderate hardware upgrades. The disadvantage of losing half the illumination intensity for each fiber group is easily offset by doubling the laser output power. This approach is generally applicable to multisite studies when the two target sites of interest are sufficiently isolated optically so that no optical cross contamination can occur from one site to the other (e.g., from one breast to the other).

The combined signal is delivered via fiber optodes to the tissue under study, with approximately 20 mW of optical power administered over an interval of 10 ms, generating a flux density of $\sim 10 \text{ mJ s}^{-1} \text{ cm}^{-2}$. Depending on the number of fibers used in a given measurement head, this yields a frame rate of 2 to 75 frames/s, adequate for investigation of most biological dynamics of interest.

Source illumination fibers are brought into contact with the tissue via an application-specific measuring head that also contains up to 32 fiber bundles for light collection. Figure 2 shows a photograph of the measurement head used for simultaneous dual-breast measurements, with spherical silicone calibration

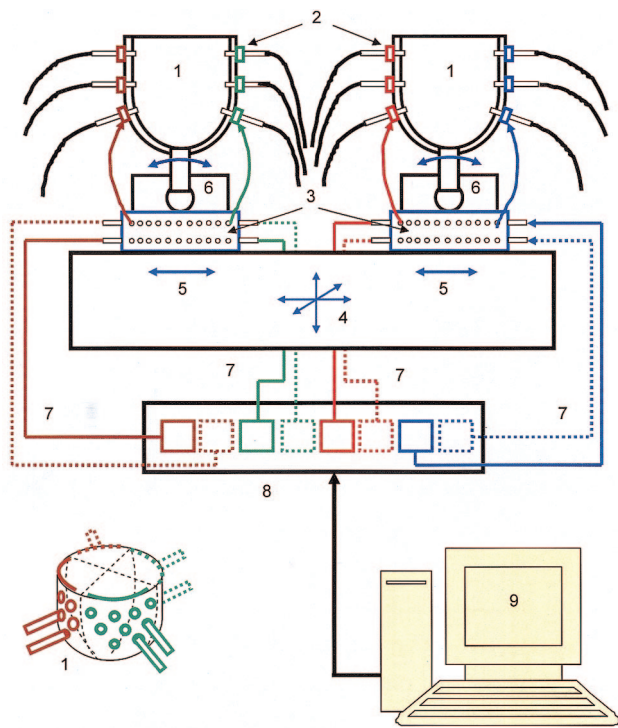


Fig. 3. Schematic of the dual-breast measuring head: 1, measuring cups; 2, fiber collets (pneumatic actuators) with optical fibers; 3, pressure manifolds; 4, 5, translation stages; 6, individual pitch and yaw adjustments; 7, pressure lines; 8, bank of voltage-controlled pressure regulators; 9, PC programmable analog voltage output card.

phantoms in place. In this case, 31 bifurcated source-detector fibers are spatially distributed over a hemispheric region of breast tissue. Each fiber optode is held in place by a supporting metal collet that incorporates the capability for pneumatic adjustment of optode position. The fibers in the dual-breast measurement head are arranged so that source fibers are sequentially illuminated during the scan in a mirror-symmetric fashion with respect to the midline of the measurement head; this minimizes the effects of cross talk between right and left breasts. Figure 3 shows a schematic representation of the same measuring head. A primary three-axis translation stage (4) allows gross positioning of the device, and additional translation (5) and tilting (6) stages allow the individual alignment of the breast cups (1). The pressure actuators (2) for the fiber optics are connected to manifolds (3) distributing air pressure from a bank of eight voltage-controlled regulators (VCR, 8) to allow independent adjustment of four groups of fibers on each cup (see inset). The voltages for the VCRs are controlled by a personal computer (PC) using a LabVIEW programmable analog voltage output card (9).

The detection fibers from each measurement head terminate in a programmable multichannel optical detector (PMOD), the individual detector channels of which are simultaneously interrogated in parallel in order to maximize system speed. For the dual-breast imager, two PMODs, one for each breast, are em-

ployed. To accommodate the large variability in signal strength seen by the detector during a source scan, each channel—defined by an active illuminating source fiber *s* and detector module *d*—is individually digitally addressed by the host PC during the measurement and directed to assume one out of seven possible sensitivity settings. This allows for compensation of signal variations over a $1:10^9$ dynamic range. The detector amplifier sensitivity settings are switched “on the fly” in synchrony with the optical switch position and are a function of the geometry of the tissue under study. Implementation of a narrowband lock-in amplifier scheme (with up to four lock-in amplifiers per detector channel) allows for detection of the frequency-encoded optical wavelengths, improving the overall signal-to-noise performance of the instrumentation. Details of the detection electronics and the gain switching scheme and system timing have been described in Ref. 2.

B. Software

The most fundamental set of software algorithms directs the activity of CPU 1 in Fig. 1 and is transparent to the user; these software routines orchestrate the timing of source switching, detector channel sensitivity settings, data acquisition, and storage (2). A second, higher level of software routines (also resident in CPU 1) is implemented in the National Instruments LabVIEW language. These routines comprise an instrument setup based on a graphical user interface (GUI), data display, and a variety of diagnostic tools. This level, the main interface through which the user interacts with the imager, consists of a setup screen (3) and a measurement screen (4), which provides real-time data display during measurement acquisition. A second CPU is available for image reconstruction (5), data analysis (6), and the display of time series of two-dimensional or three-dimensional volume-rendered reconstructed images (7).

Figure 4 shows the instrument setup screen. Compared with earlier (i.e., 32-S by 32-D) versions of the software, this user interface was modified to accommodate the increased number of measurement channels. Instead of populating the screen with the control elements for all detector channels as done in previous systems, the dual-site imager has a channel selector (2) to choose a source-detector pair of interest for manual adjustment (3a and 3b). Before a measurement, it is necessary to establish the detector gain settings for each source-detector combination to configure the imager for a specific target. This task is performed by an automated gain setup feature in the setup screen, which records signal levels from each detector channel while stepping through the available gains. Based on a decision-making algorithm, those gains that promise the best signal-to-noise ratio without risking detector saturation are kept stored for the measurement. This algorithm and the principle of dynamic gain adjustment are identical to those described for a single-site setup.² The gains for both

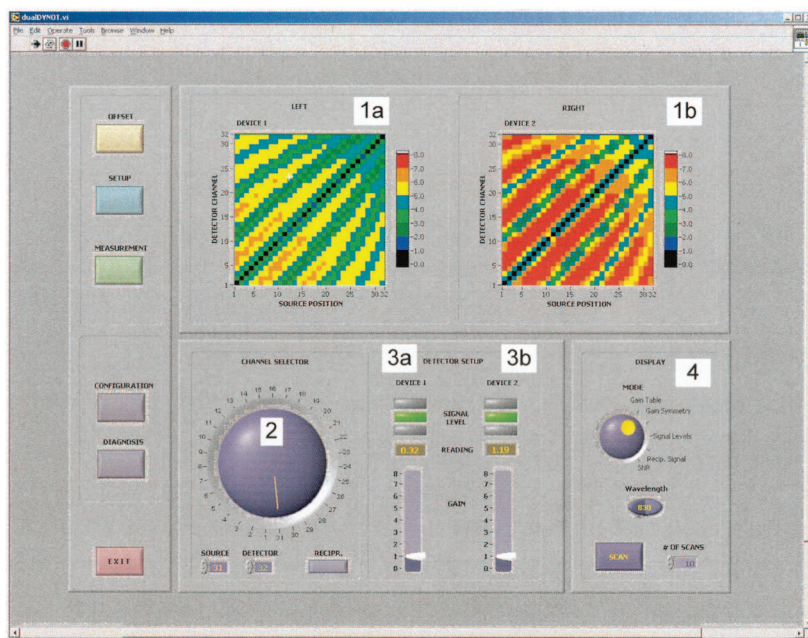


Fig. 4. Dual-breast setup screen. 1a, 1b, Displays for various data integrity measurements [shown here, color-encoded gain setting tables for left breast (a) and right breast (b)]. 2, Source–detector channel selector for manual gain adjustment. 3a, 3b, Gain selectors and signal displays for manual gain adjustment. 4, Selection of checkout algorithm results to be displayed in 1a and 1b.

PMODs are adjusted independently. The automated gain adjustment usually yields satisfactory results for the majority of channels, and manual readjustment typically is required for only a few isolated channels.

Multiple data integrity checks, described in detail below, are integrated into the interface to provide the operator with immediate feedback about hardware status and quality of experimental setup during preparation of a measurement. Two displays (1a and 1b), one for each breast, show the results of the available system setup checks (4) to alert the user to possible problems in the measurement setup, such as bad fiber–tissue contact, erroneous gain settings, or hardware degradation. Shown in Fig. 4 is a display of color maps representing the gain settings for all sources and detectors for both breasts. Pixels appearing in blue, such as those along the main diagonals of the displays, represent low gain settings corresponding to small S–D separation, and colors toward the red end of the spectrum represent the higher gains expected for large S–D separation. A characteristic pattern evolves, which depends on the measurement geometry. The pattern seen here is characteristic for the measuring head shown in Fig. 2. The screens in Fig. 4 were obtained with the two homogeneous spherical phantoms depicted in Fig. 2. The difference in gain settings for left versus right is explained by the fact that the phantom in the right breast position (right display, 1b) is optically denser and therefore requires a larger fraction of high gain settings.

3. Evaluation of Data Integrity

As the number of source–detector channels increases, so do system complexity and the sizes of

resulting data files. As a consequence, it becomes impractical to manually evaluate individual data channels for measurement errors, and automated error-checking routines become a necessity. Our approach to evaluation of data integrity examines dynamic changes in reciprocal data channels, i.e., pairs of source–detector channels for which source and detector are interchanged. In the ideal case, one expects identical data signals in the channels constituting a reciprocal pair, given that the absorption and scattering properties of a medium are independent of the direction of light propagation. That is, the near-infrared signal detected when source fiber m is illuminating the tissue and detector fiber n is sensing the transmitted optical energy should be identical to the signal obtained when fiber n illuminates and fiber m detects. This capability is possible because of our use of a nested optode arrangement wherein each fiber bundle consists of a central core (1-mm diameter) of illuminating fibers surrounded by a halo of receiving fibers.

Optode-to-subject contact is a critical parameter in determining the fidelity of the near-infrared measurements recorded during a tomographic experiment. Poor contact between an optode fiber and the subject will have a far greater effect when the fiber in question acts as a detector than when it is a source, owing to the expected Lambertian directional dispersion of optical energy exiting the tissue. Thus, for pairs of reciprocal fibers (m, n), poor contact for fiber m will result in significantly greater signal reduction in source–detector channel nm (where m acts as the detector fiber) than in channel mn (where n acts as the detector fiber). A comparison of the signals detected in reciprocal channels can thus allow one to

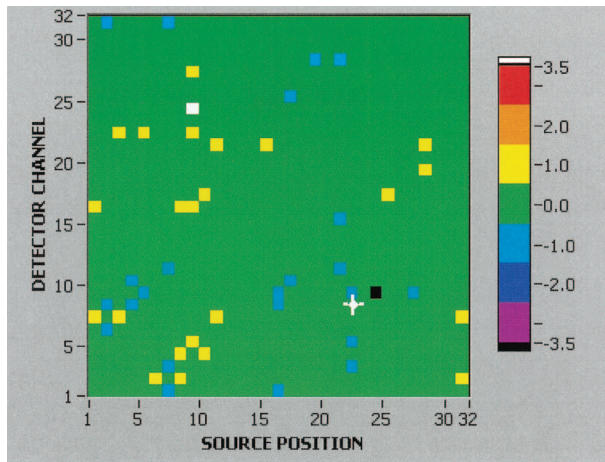


Fig. 5. Screen shot of the gain symmetry check offered by the system setup screen. Differences in reciprocal gain settings of ± 1 are permissible. In this example, the gain for S24/D9 requires readjustment.

draw inferences regarding the integrity of optode contact.

Data integrity procedures are largely automated to allow for nearly real-time evaluation of hardware function and instrument setup immediately prior to a physiologic experiment. System integrity checks are integrated in the LabVIEW GUI and have been merged into the setup screen to enhance system usability.

A. Gain Symmetry

The graphic representation of gain settings, as illustrated in Fig. 4, shows a characteristic pattern that depends on the target geometry and the optode arrangement. Deviations from the pattern are indicative of inadequate gain settings, but individual affected channels are difficult to discern in the complicated structure of the gain display. Therefore, the setup screen provides a function that calculates the difference between gain steps for reciprocal channels and displays the color-coded result. Ideally, reciprocal signal levels and therefore the required gain would be identical. In practice, however, the signal levels are not exactly equal owing to variations in optical losses and optical coupling efficiencies for the different source–detector pathways. Because of this and because the dynamic measurement range for neighboring gain settings overlap to some extent, a difference of one gain step is regarded as permissible. Gain step differences of two or more call for operator attention. Inadequate gain settings in a few isolated channels are encountered occasionally and typically are the result of the automated setup algorithm’s not being capable of settling for a gain. An example for this case is illustrated in Fig. 5. If inadequate gain is established, the operator can select the channel in question for closer inspection and for manual gain readjustment. Clusters or line structures of channels showing gain asymmetry are indicative of degraded optical contact due, for example, to patient motion.

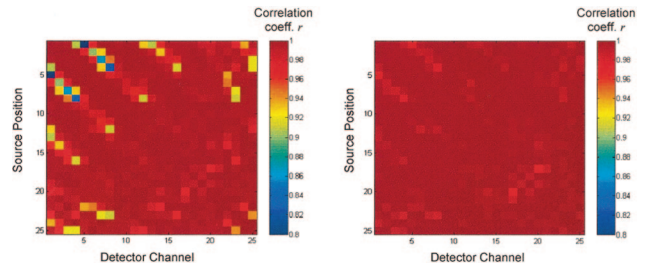


Fig. 6. Example of reciprocal channel cross correlations, calculated for a 25-source measurement head. Left panel, raw, unfiltered data; right panel, filtered data. Color scales range from $r = 0.8$ to 1.0.

The gain symmetry test is a robust and important first step to confirming that the measurement setup is basically correct.

B. Channel Reciprocity Calculations

Implementation of an automated scheme for assessing data integrity based on source–detector channel reciprocity requires a brief collection of DYNOT data. The collected signal typically contains dynamic content resulting from an external provocation used to induce hemodynamic variations (e.g., pneumatic cuff inflation of the upper arm or a Valsalva maneuver). The intent of these variations is to introduce nonrandom fluctuations in the near-infrared signal detected during the measurement to assess signal fidelity in reciprocal source–detector channels.

The presence of poor fiber contact typically will introduce signal distortion and degradation in the signal-to-noise ratio, affecting reciprocal source–detector channels in an unequal manner, as discussed above. Thus all pairs of reciprocal channel time series can be identified, and a correlation coefficient r can be computed for each such pair.

A reciprocal pair of channels having no distortion will exhibit a correlation coefficient near unity ($r \cong 1$), while reciprocal channels containing (asymmetric) distortion will have correlation coefficients less than one ($r < 1$), with a value decreasing toward zero as the distortion worsens.

In practice, any pair of reciprocal channels will be uncorrelated to some extent owing to unavoidable random noise fluctuations. These fluctuations will have greater amplitude for channels with higher detector amplifier gain settings, corresponding to the longer optical path lengths in tissue. To mitigate the effect of these fluctuations on reciprocity calculations, we typically perform the calculation twice: once on raw data, and a second time on data that has been low-pass filtered (with a user-specified cutoff frequency). A correlation coefficient that is low owing to noise will generally increase toward unity after filtering, while systematic measurement errors (e.g., due to poor optode contact) will result in a correlation coefficient that is little affected by filtering.

As an illustration of the assessment scheme, Fig. 6 shows a map of correlation coefficients for reciprocal channels, for an experiment with good optode contact

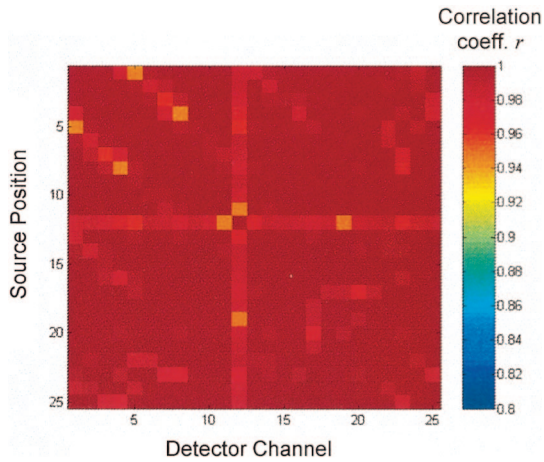


Fig. 7. Low-pass filtered reciprocal channel cross correlations for the same measurement head as in Fig. 6, with poor target contact for detector fiber 12.

and high measurement fidelity, performed using an older 25-detector breast measurement head design. In this figure, the left panel shows the correlation coefficients for raw data, and the right map shows the correlation coefficients for data that have been low-pass filtered with a cutoff frequency of $0.12 * f_N$, where f_N is the Nyquist frequency (for this example, 1.25 Hz). The dark red points in the left panel have correlation coefficients near unity, while those points toward the blue end of the scale correspond to source-detector channels with deeper tissue penetration, longer optical path lengths, and consequently higher signal-to-noise ratios. The distribution of these lower-correlation points has a characteristic appearance for each measurement head design. The random noise contribution in these channels—which results in correlation coefficients lower than unity—is decreased by low-pass filtering, and the postfiltered map on the right shows these correlation coefficients increasing toward unity. Note that the map is symmetrical about the main diagonal owing to the fact that, for the reciprocal source-detector pairs (a,b), the correlation coefficients r_{ab} and r_{ba} are equal.

Figure 7 shows a similar plot of correlation coefficients for a case in which an optical fiber (in this case, fiber 12) makes poor contact with the breast. Even with low-pass filtering, it is evident that certain correlation coefficients deviate from unity; the “cross” appearance in the map indicates that all reciprocal pairs consisting of channels for which fiber 12 is either the detector or the source suffer from a reduced correlation coefficient arising from the poor contact of that fiber. This scheme thus offers an approach by which a poorly contacting fiber may be directly and immediately identified at the time of measurement. It has been our experience that cross patterns having r values less than 0.9 deserve operator attention.

C. Root-Mean-Square Difference Calculations

In certain cases computation of the correlation coefficient is not sufficient for identification of systematic

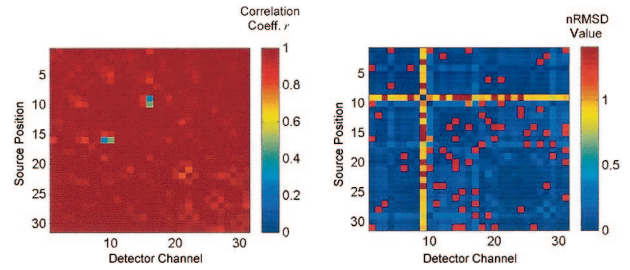


Fig. 8. Example of reciprocal channel cross correlations and normalized RMS differences, calculated for a 31-source measurement head, with an offset error in fiber 9. Left panel, reciprocal channel cross correlation; right panel, reciprocal channel RMS difference computation, both low-pass filtered.

errors in experimental data. A case of particular interest occurs when a constant detector offset voltage appears in one source-detector channel of a reciprocal pair but not in the other channel. In this case, the correlation coefficient computation will be unaffected by the constant offset and thus will be unable to identify this systematic error.

To identify this particular type of systematic error, consider two time series that constitute a reciprocal source-detector pair, each having a length of N time points: X_i and Y_i , $i = 1, \dots, N$. We compute the following normalized root-mean-square (RMS) difference between these two time series:

$$\text{nRMSD} = \frac{\left[\frac{1}{N} \sum_{i=1}^N (X_i - Y_i)^2 \right]^{1/2}}{\left[\frac{1}{N} \sum_{i=1}^N \left(\frac{X_i^2}{2} + \frac{Y_i^2}{2} \right) \right]^{1/2}}, \quad (2)$$

where the summation index ranges over the series length N . The quantity computed in Eq. (2) is bounded and has two interesting special cases: $\text{nRMSD} = 2^{1/2}$ if exactly one of the time series is identically zero, and $\text{nRMSD} = 2$ if $X = -Y$. This computation will identify those reciprocal pairs exhibiting a constant systematic offset error. Figure 8 illustrates cross-correlation and nRMSD maps for a breast measurement head having 31 source-detector fibers. In this case, fiber-detector 9 exhibits a constant offset error. The correlation coefficient map on the left fails to identify the fiber whose detector offset voltage is incorrect; while poor reciprocity between channels S9/D16 and S16/D9 is evident, which of the two involved fibers is the problematic one cannot be identified. The nRMSD map on the right, on the other hand, clearly identifies offset error as the problem and indicates that fiber 9 is the problematic one.

The gain symmetry, correlation coefficient, and nRMSD calculations allow the identification of possible data corruption due to unreliable fiber-tissue contact, improper gain setup, or hardware malfunction. It is important to have these automated capabilities for two reasons. First, it is the only feasible way to perform a thorough checkout for the large number of data channels (here, 2 sites at 2 WL

$\times 31 \text{ S} \times 31 \text{ D} = 3844$) for each measurement in a timely fashion. Second, the described checkout procedures provide objective performance acceptance criteria for instrument operation.

It is worth emphasizing that these checkout procedures, all of which are based on signal reciprocity, are available only because of the particular optode geometry of the instrument, which employs collocated source and detector positions. We are able to use this optode geometry only because of the large dynamic detection range offered by source time multiplexing in combination with dynamic gain adjustment.

4. Methods

The human studies presented here were performed under an Institutional Review Board–approved protocol (99-093) at University Hospital of the State University of New York's Downstate Medical Center, Brooklyn. After the subjects gave their informed consent, they were trained to perform a controlled Valsalva maneuver, for which they were asked to maintain a fixed exhalation pressure of 40 mmHg for a given period of time, ideally 40 s. To monitor exhalation pressure, the volunteers were asked to breathe out into a fixed-volume vessel to which a pressure gauge was connected. The subjects were then asked to lie in a prone position on the breast imager gantry with their breasts hanging pendant through an opening above the dual-breast imaging head, as schematically indicated in Fig. 2. Their comfort was ensured by using pillows and blankets for positioning as necessary. The subjects were informed about the importance of avoiding even small movements because of their possible interference with the measurements.

After stable positioning of the subject was ensured, the measuring head was raised and the breasts were carefully positioned inside the measuring cups. Care was taken to bring the cups as close to the chest wall as possible and to encompass the entire volume of the breast. The optical fibers were then gently adjusted to make contact with the breast, all the while querying the subject to avoid any discomfort.

At this point, automated gain adjustment was initiated, followed by the sequence of reciprocity checks outlined above, with adjustments to the setup made as necessary. Once satisfactory results were obtained, a baseline measurement was performed for a period lasting 5–10 min with the subject at rest. Next the subject was asked to perform a series of Valsalva maneuvers, typically three, each lasting up to 40 s, separated by 5-min recovery periods.

The collected data were subjected to a series of preprocessing steps that served to suppress noise and to correct for the influence of laser power fluctuations and to reject data channels that showed excessive noise. These data, normalized to the mean of the baseline period, were subsequently evaluated to reconstruct a three-dimensional image time series for each illumination wavelength using the normalized-difference method as described previously.⁹ From these, relative changes in hemoglobin (Hb) levels were computed, using methods described in Ref. 10.

Where appropriate, the image time series was also subjected to analysis using various standard signal processing routines for extraction of dynamic metrics (e.g., signal separation techniques, time–frequency, rate analysis, etc.) using recently reported software applications.¹¹

5. Results

A. Example Clinical Results

To evaluate the functioning of the dual-breast imaging setup and to demonstrate its clinical usefulness, we have begun conducting physiologic breast studies on healthy volunteers and on individuals with a history of breast cancer; some exemplary results are presented below.

As further motivated in Subsection 5.B below, we chose repeated controlled Valsalva maneuvers to invoke transient venous congestion in the breast.^{7,12} Figure 9 shows the measuring screen with simultaneous data display for both breasts in real time during one Valsalva epoch performed by a patient bearing a 6-cm ductal carcinoma in her left breast. Shown is the color-encoded representation of the relative variation in intensity transmitted through the tissue for each S–D combination (vertical axis) and its progression over time (horizontally scrolling axis).

A marked difference between the breasts is seen in the raw data. The lower display—corresponding to the left (tumor-bearing) breast—shows a significantly slower recovery from the Valsalva maneuver. The raw data also suggest a spatially less homogeneous recovery to baseline for the left than for the right breast.

Figure 10(a) shows the temporal variations of the means of the deoxyhemoglobin (Hb_{red}) signals averaged across all S–D channels for each measuring head for the same Valsalva epoch shown in Fig. 9. The changes in the Hb_{red} signals, with respect to the average value during the baseline measurement period, were estimated from the dual-wavelength normalized detector readings by applying a modified Beer–Lambert law (MBL), which assumes equivalent optical path lengths for both wavelengths. The estimation procedure, described in detail in Appendix A, yields a quantity proportional to the product of Hb state concentration change and the distance that light travels in propagating from source to detector. Because the latter is unknown, the plotted concentration changes are given in arbitrary units. We use this estimated quantity for Hb state changes throughout this paper.

Detector channels with excessive noise (baseline-period coefficient-of-variation values $>20\%$) were excluded from the mean-value calculation. We show the Hb_{red} signal because it is most sensitive to the modulation of the venous return caused by the Valsalva stimulus. The tumor-bearing breast clearly shows an overall more sluggish response to the maneuver, with a slower onset and a prolonged return to the baseline. In addition, the response magnitude appears reduced for the tumor breast. The result is consistent with the

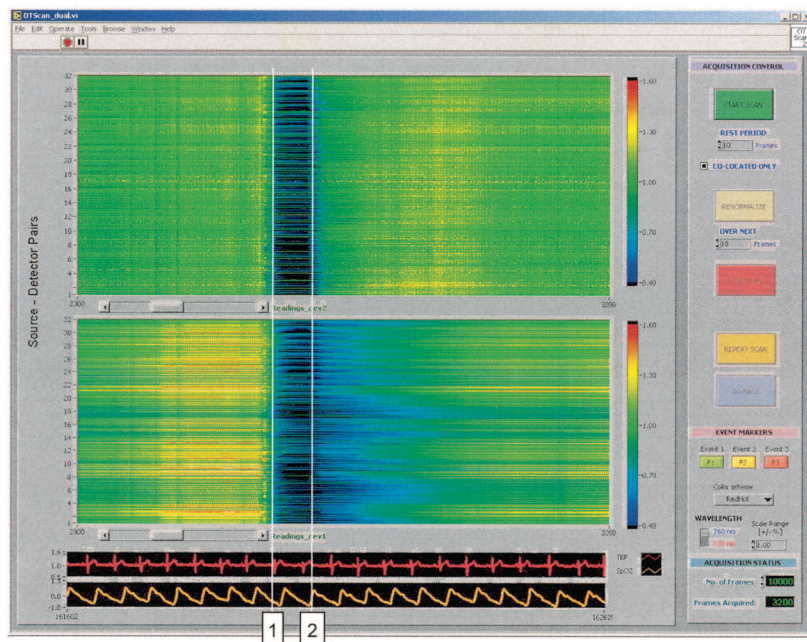


Fig. 9. Screen shot of the dual-breast measurement screen during data acquisition, showing raw data time series for left (bottom, cancerous) and right (top, healthy) breast at 760 nm. Displayed are the color-encoded transmitted light intensity values for all data channels (vertical axis) and their change over time (scrolling horizontal axis). 1, 2, Onset and release of Valsalva, respectively. The data from the shown epoch were used to obtain results shown in Figs. 10 and 12.

well-known finding that the vascular network in neoplastic tissue has marked architectural and functional disturbances.¹³ The presence of a tumor, especially if large, can therefore be expected to affect global measures such as the spatial mean of optical signals.

Figure 10(b) shows the results from the same experimental protocol performed on a healthy individual. It can be seen that both breasts show remarkably similar response curves. The benefit of simultaneous recording of hemoglobin states becomes clear: A direct comparison of optical data recorded simultaneously from right and left breasts can serve to more readily identify pathological tissue behaviors.

Because we interpret the difference between the results seen in Figs. 10(a) and 10(b) as the disturbing effect of a tumor in otherwise largely homogeneously responding tissue, it is worthwhile to quantify the homogeneity of the healthy tissue response to see if such an assumption is warranted.

Figure 11 shows the result of a GLM (general linear model¹⁴) analysis of data for a healthy subject. Here we used the mean oxyhemoglobin (Hb_{oxy}) time series as a model function and computed the percentage of variance accounted for by this model function within each source–detector channel’s Hb_{oxy} time series. Figure 11 illustrates the results of this computation. Four curves are shown: the rank-ordered GLM percent-of-variance-accounted-for values for two consecutive Valsalva epochs for left and right breast data. The curves are notably similar across repeat Valsalva epochs, and the model function accounts for more than 90% of the variability in the data in more than 95% of all source–detector chan-

nels. We see this as evidence that healthy breast tissue indeed reacts to the stimulus in a very coherent manner.

Figure 12(a) shows reconstructed-image time-series results obtained at discrete time points during and following the Valsalva maneuver shown in Figs. 9 and 10(a). Shown are volume-rendered images of the temporal first derivative of the Hb_{red} pixel time series at the time points identified in Fig. 12(b). Pixels with positive values (colored red) indicate an increase in Hb_{red} concentration, whereas negative values (blue regions) signify a local decrease in Hb_{red} . The images in the lower row (healthy breast) appear significantly more homogeneous than the ones for the tumor breast. Image frames 3–7 in the lower row indicate falling Hb_{red} concentrations throughout the entire breast volume.

In contrast, the upper image row, calculated for the tumor-bearing left breast, identifies a heterogeneity, which coincides with the location of the tumor. Also of interest is the finding that in the tumor-bearing breast the surrounding tissue behaves in a manner qualitatively similar to the healthy tissue of the other breast. The Hb_{red} concentration at the location of the lesion increases from frames 4 through 6. This finding of focal induced transient hypoxemia is consistent with the known sluggish perfusion of solid tumors and with a previously reported finding obtained using a single breast measuring head.^{15,16} In the earlier case the maneuver involved a prolonged breathhold (60 s), which is in many aspects similar to a Valsalva maneuver. As in the current findings, evidence of induced transient hypoxemia was limited to the tumor-bearing breast.

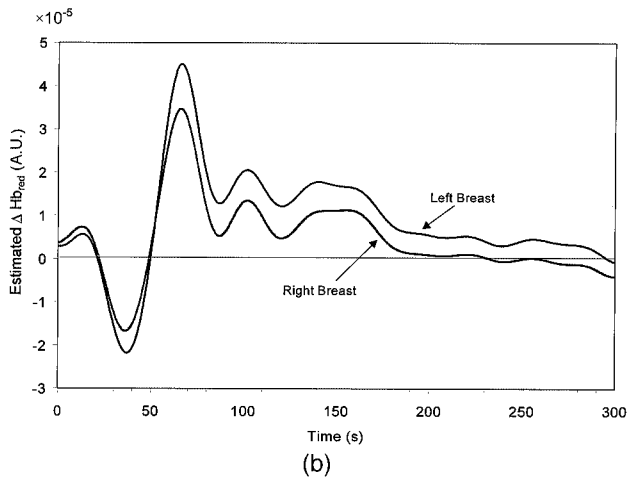
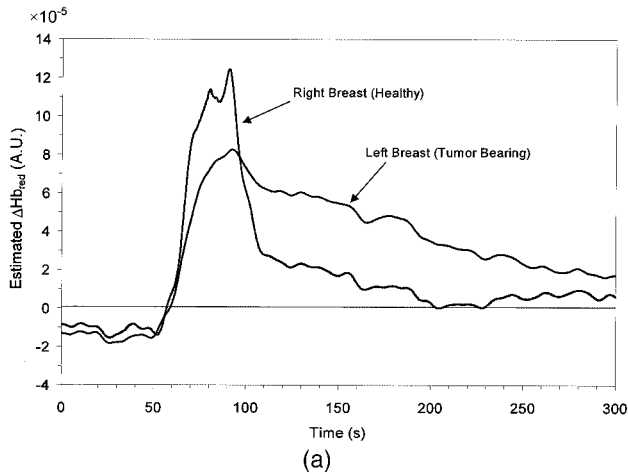


Fig. 10. Change in spatially averaged Hb_{red} concentration over time, simultaneously recorded from the left and right breasts of (a) a patient with a left-sided breast tumor and (b) a healthy individual. The subjects were asked to perform a Valsalva maneuver during the shown epoch of the experiment.

B. Experimental Considerations and Repeatability

An important aspect in the implementation of a dual-breast measurement system is the design of an experimental protocol and a firm understanding of how experimental variables interact with the hardware to affect the fidelity of the collected data. A poorly designed protocol will result in data that are unacceptably sensitive to small variations in experimental setup and that are difficult to replicate. DYNOT imaging achieves an advantage over static techniques by allowing the investigator to observe real-time dynamic variations in collected data.

In addition, the simultaneous bilateral approach implemented here provides a basis for additional sensitivity. However, the practical realization of these advantages depends on the availability of a protocol that provides for consistent findings. To explore this, we have conducted a series of investigations to determine the influence of subject-dependent variables on the quality of data collection. These variables include, but are not limited to, involuntary movement (e.g.,

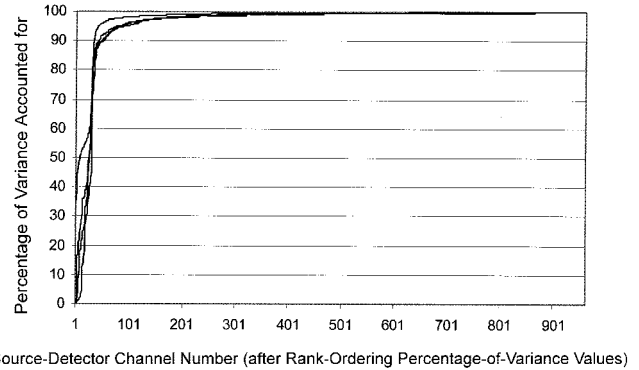


Fig. 11. Rank-ordered GLM percentage-of-variance values for source–detector channel Hb_{oxy} time series, using the spatially averaged Hb_{oxy} time series as a model function. Four curves correspond to Valsalva maneuver epochs 1 and 2, for left and right breasts.

coughing during the experiment), subtle changes in limb or body position, repositioning to minimize discomfort, and shifting of head orientation while lying prone during the experiment. These variables may produce artifactual changes in measured data that may be of the same order of magnitude as the dynamic changes induced by an externally imposed provocation that forms part of the experimental protocol.

As an example, Fig. 13 illustrates the spatially averaged Hb_{oxy} time series recorded from a healthy volunteer, simultaneously acquired from left and right breasts. During the experiment, the patient performed two Valsalva maneuvers separated by approximately 600 time points (316 s), after which she was asked to turn her head from its original left-facing orientation toward the right. She subsequently completed two additional Valsalva maneuvers separated by approximately 600 time points. It can be seen that head orientation has a significant influence on average Hb_{oxy} concentration; the simple act of reorienting the head from left to right results in a abrupt change in Hb_{oxy} concentration (at approximately time point $1790 \cong 942$ s). The change is positive for the right breast and negative for the left breast, and it is most likely due to changes in compression of the carotid sheath, leading to changes in circulatory flow dynamics within the breast parenchyma.

Reorientation of the head results not only in abrupt changes in the baseline value of Hb_{oxy} , but it also affects the magnitude of changes in hemoglobin signals in response to external provocations such as a Valsalva maneuver. Prior to head reorientation, the left breast Hb_{oxy} signal shows a greater change during Valsalva than does the right breast signal. After orientation of the head toward the right, the right breast Hb_{oxy} signal shows a greater response to the external provocation.

Knowledge of such subject-dependent variables is important in the design and standardization of experimental protocols, as careful attention should be

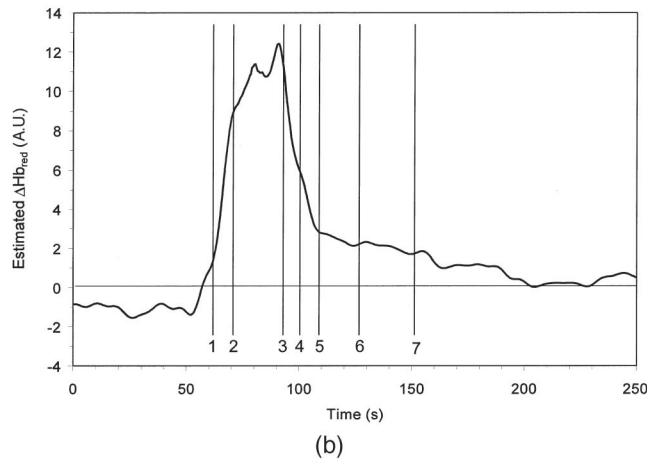
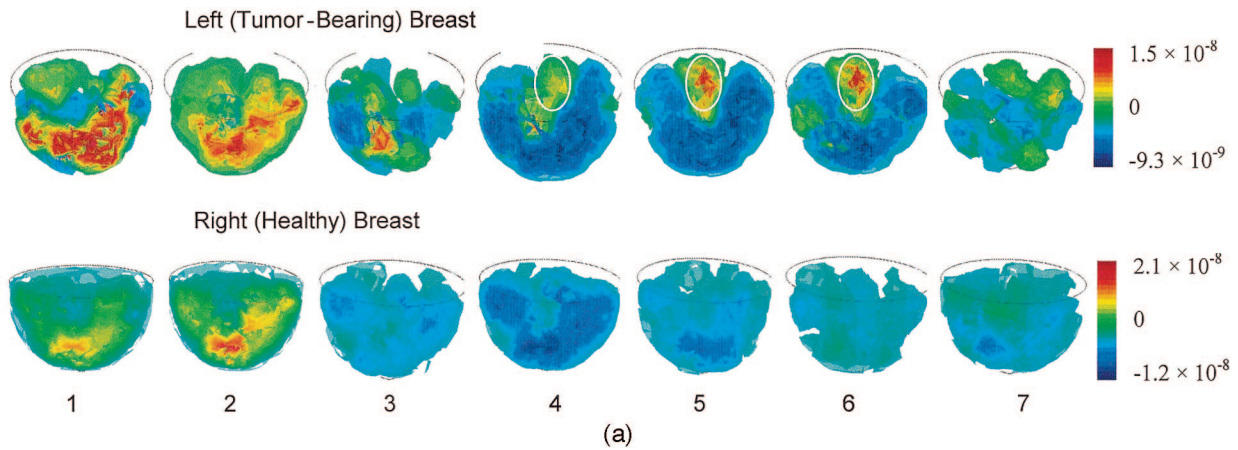


Fig. 12. Panel (a), reconstructed volumetric image time series of the change in Hb_{red} during a Valsalva maneuver. Top row, left breast with tumor; bottom row, healthy right breast. The approximate location and size of a ductal carcinoma, as known from radiologic findings, is indicated. Panel (b), spatial mean of reconstructed changes in Hb_{red} for the healthy breast. Numbers indicate the approximate location of time points for the reconstruction results.

paid to minimizing the effect of these variables on data analysis. In this case, it can be desirable to choose data analysis techniques that are insensitive to relative magnitudes of dynamic behavior; for example, a GLM analysis performed on left breast data

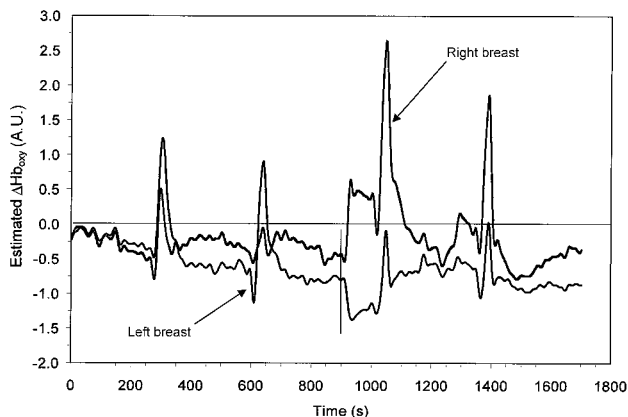


Fig. 13. Temporal variation in the spatially averaged Hb_{oxy} signal as a function of time. (Healthy volunteer performing four Valsalva maneuvers, with a head turn at 900 s.)

could employ a model function also derived from left-sided spatially averaged signals.

Thus, in dynamic tomographic imaging, patients must be informed of the consequences of relatively small, innocent movements to make them aware of their potential effect on results. Encouraging a patient to lie as still as possible and remain silent throughout the experimental duration as well as ensuring patient comfort prior to the experiment will minimize the deleterious effects of motion artifact.

In addition to guiding the development of the experimental protocol, studies of subject-dependent factors help to improve design of system hardware such as the gantry or the measuring head. For example, the described head-turn study stimulated the design of a doughnut-shaped head rest similar to those found in massage chairs. This will allow a straight-ahead position and the equal and stable perfusion of both measurement sites.

6. Conclusions

Implementation of a system for simultaneous bilateral near-infrared optical measurements allows for the determination of physiologic detail that has been

heretofore unavailable; however, this capability necessarily comes at the cost of greater complexity. Increased system complexity—a function of the number of discrete illumination wavelengths and the number of source–detector fibers—in turn requires the incorporation of automated software algorithms for evaluation of data integrity and error checking. As a consequence, we have developed a suite of automated, real-time data integrity checks that identify data channels prone to corruption due to either faulty system setup, such as inadequate gain settings or bad tissue–fiber contact, or to hardware problems such as damaged or dirty optical fibers or malfunctioning detector electronics. A computation of reciprocal channel correlation coefficients and normalized RMS differences permits immediate identification of specific source–detector optical fibers suffering from poor contact fidelity at the fiber–tissue interface, allowing for measurement head adjustment prior to initiation of data collection. These tests, performed before each measurement, also pinpoint detector channels with inadequate gain settings to allow for manual gain correction.

Initial clinical trials on healthy volunteers and cancer patients demonstrate the usefulness of simultaneous bilateral optical breast measurements. We have demonstrated marked differences between the responses of the cancerous and healthy breasts in a patient, which can be observed in the raw data, in global measures such as spatially averaged hemoglobin states, and in reconstructed image time series. The breasts of healthy individuals, in contrast, show a much more homogeneous and similar behavior, as demonstrated by a GLM analysis.

Careful design of an experimental protocol for dynamic near-infrared tomographic imaging is necessary to ensure that measurement results are repeatable and free of hardware artifacts. For example, we established a controlled Valsalva maneuver by using a modified spirometer for subject feedback. Model-based signal separation techniques applied to source–detector data can be used to verify that collected data are consistent and repeatable.

Experimental trials in which subject position (e.g., head direction) is varied during the course of the measurement reveal the high sensitivity of the instrumentation to small changes in hemodynamics, and suggest the importance of careful attention to subject-dependent variables. Given that measurement artifacts in the data—resulting from involuntary movements or subtle changes in position or orientation—may have a magnitude comparable with physiologic dynamics, care has to be taken to avoid such artifacts.

To achieve satisfactory repeatability of the provocation maneuvers and to minimize motion artifacts, we train the subjects on the Valsalva maneuver and inform them of the importance of lying still. Artifact studies also serve to guide the design of patient interface hardware such as the gantry and the measuring head. Future developments based on such studies include the design of a more ergonomically shaped

gantry and several adjustable rests for feet, hips, and head that help bring the patient into a stable, comfortable resting position.

Appendix A

Here we present a summary of the data normalization procedure used in generating hemoglobin-concentration time series such as those in Figs. 10, 12(b), and 13.

As is common practice in near-infrared spectroscopy applications, the computations of volume-averaged hemoglobin concentrations presented here are based on a modified Beer–Lambert law (MBL).^{17,18} An important practical difference between our MBL formulation and those of most other groups is that the former uses changes in detector response, relative to an initial or baseline value, as its input data. One advantage of this approach is that precise calibration of source and detector efficiencies, while possible,¹⁹ is not required. However, in the absence of calibrated absolute light intensities, it is not possible to derive quantitatively accurate volume-averaged hemoglobin concentrations.

The mathematical form of the MBL^{17,18} is

$$I = I_0 \exp[-(\overline{\mu_a}d + A_0)], \quad (\text{A1})$$

where I_0 and I denote the intensities of light at the illumination and detection positions, respectively; $\overline{\mu_a}$ is the average absorption coefficient in the volume of tissue that is illuminated by the scattered photons; d is the “mean-average” distance light travels inside the medium²⁰; and A_0 is a “geometry factor” that accounts for the reduction in light intensity that would occur even if the medium were nonabsorbing.^{18,19} Setting $\overline{\mu_a} = 0$ in Eq. (A1) gives $I^0 = I_0^0 \exp[-A_0]$, where superscript zeros denote intensity values for a nonabsorbing medium. Then in the general case the volume-averaged absorption can be solved for as

$$\frac{1}{d} \ln \left(\frac{I^0 I_0}{I_0^0 I} \right) = \overline{\mu_a}. \quad (\text{A2})$$

However, in practice, the distance d is not empirically measurable,²¹ and so it is moved to the right-hand side of Eq. (A2), and the latter is rearranged to

$$\ln \frac{I(t)}{I_0(t)} = \ln \frac{I^0(t)}{I_0^0(t)} - \overline{\mu_a}(t)d, \quad (\text{A3})$$

where we have also introduced an explicit time dependence, because the measurements are dynamic, as the final form of the MBL. Equation (A3) is arranged so that quantities that are not directly observable are on the right-hand side and are related to the ratio I/I_0 , which is experimentally measurable.

It is recognized that if the medium’s absorption varies in time, then presumably the distance d does

also. However, as shown below, strong positive correlations have been obtained between hemoglobin time series derived from detector data using the MBL and hemoglobin time series computed from reconstructed images, indicating that errors resulting from temporal variations of d and from violations of other basic assumptions (i.e., approximately homogeneous μ_a and exponential attenuation with increasing d) can safely be neglected.

The detector preprocessing referred to in Section 4 above has two steps. First, each raw detector value is normalized to the laser-intensity reference value measured at the same time; there are unknown coupling efficiency factors associated with both, giving a ratio of $[kI(t)]/[k_0I_0(t)]$, where k is the coupling efficiency for the detector reading and k_0 is that for the laser-intensity reference value. In the second step, each instantaneous $[kI(t)]/[k_0I_0(t)]$ value is normalized to the mean value of $[kI(t)]/[k_0I_0(t)]$ during a defined baseline period and for the same source-detector channel. The resulting time-varying parameter $x(t)$, where

$$x(t) = \frac{kI(t)}{k_0I_0(t)} \bigg/ \frac{\sum_{t_1}^{t_2} kI(t)}{\sum_{t_1}^{t_2} k_0I_0(t)} = \frac{(t_2 - t_1 + 1)kI(t)}{k_0I_0(t) \sum_{t_1}^{t_2} k_0I_0(t)} \quad (\text{A4})$$

is the normalized detector reading that is the input data for both the MBL and the image-reconstruction operations. Equation (A4) is equivalent to

$$\begin{aligned} \ln x(t) &= \ln(t_2 - t_1 + 1) + \ln \frac{k}{k_0} - \ln \sum_{t_1}^{t_2} \frac{kI(t)}{k_0I_0(t)} + \ln \frac{I(t)}{I_0(t)} \\ &= \left[\ln(t_2 - t_1 + 1) + \ln \frac{k}{k_0} + \ln \frac{I^0(t)}{I_0^0(t)} \right. \\ &\quad \left. - \ln \sum_{t_1}^{t_2} \frac{kI(t)}{k_0I_0(t)} \right] - \overline{\mu_a(t)d} \\ &= \left[\ln(t_2 - t_1 + 1) + \ln \frac{I^0(t)}{I_0^0(t)} - \ln \sum_{t_1}^{t_2} \frac{I(t)}{I_0(t)} \right] \\ &\quad - \overline{\mu_a(t)d} \\ &\equiv K - \overline{\mu_a(t)d}, \end{aligned} \quad (\text{A5})$$

where Eq. (A3) is substituted into the last term on the right-hand side of the first line of Eq. (A5) and K is defined as the bracketed expression in either the second or third line of Eq. (A5). The cancellation of k and k_0 between the second and third lines is based on an assumption that these coefficients are constant during the time course of a measurement, that is, that there is no change in probe contact during the data collection.

The instrument described in this paper performs simultaneous measurements at two wavelengths, so a numerical subscript is appended to the final result

in Eq. (A5) as a wavelength index:

$$\begin{aligned} \ln x_1(t) &= K_1 - \overline{\mu_{a1}(t)d_1}, \\ \ln x_2(t) &= K_2 - \overline{\mu_{a2}(t)d_2}. \end{aligned} \quad (\text{A6})$$

Estimates of tissue-volume-averaged Hb_{oxy} and Hb_{red} concentrations— \bar{c}^o and \bar{c}^r , respectively—are derived from the two-wavelength absorption coefficients by computing the linear combinations

$$\bar{c}^o = \frac{\varepsilon_2^r \overline{\mu_{a1}^r} - \varepsilon_1^r \overline{\mu_{a2}^r}}{\varepsilon_2^r \varepsilon_1^o - \varepsilon_1^r \varepsilon_2^o}, \quad (\text{A7})$$

and

$$\bar{c}^r = \frac{\varepsilon_1^o \overline{\mu_{a2}^r} - \varepsilon_2^o \overline{\mu_{a1}^r}}{\varepsilon_1^o \varepsilon_2^r - \varepsilon_2^o \varepsilon_1^r}, \quad (\text{A8})$$

where the ε symbols denote the molar extinction coefficients for the indicated oxygenation states of hemoglobin at the indicated wavelengths. The true values of μ_{a1} and μ_{a2} are not known, and so $-\ln x_1(t)$ and $-\ln x_2(t)$ are used as approximations to them. Substituting Eq. (A6) into Eqs. (A7) and (A8) leads to

$$\begin{aligned} \frac{\varepsilon_2^r [\overline{\mu_{a1}(t)d_1} - K_1] - \varepsilon_1^r [\overline{\mu_{a2}(t)d_2} - K_2]}{\varepsilon_2^r \varepsilon_1^o - \varepsilon_1^r \varepsilon_2^o} &= \frac{\varepsilon_1^r K_2 - \varepsilon_2^r K_1}{\varepsilon_2^r \varepsilon_1^o - \varepsilon_1^r \varepsilon_2^o} \\ &+ \frac{\varepsilon_2^r \overline{\mu_{a1}(t)d_1} - \varepsilon_1^r \overline{\mu_{a2}(t)d_2}}{\varepsilon_2^r \varepsilon_1^o - \varepsilon_1^r \varepsilon_2^o} \\ &= K_3 + \frac{\varepsilon_2^r \varepsilon_1^o d_1 - \varepsilon_1^r \varepsilon_2^o d_2}{\varepsilon_2^r \varepsilon_1^o - \varepsilon_1^r \varepsilon_2^o} \bar{c}^o + \frac{\varepsilon_1^r \varepsilon_2^r (d_1 - d_2)}{\varepsilon_2^r \varepsilon_1^o - \varepsilon_1^r \varepsilon_2^o} \bar{c}^r, \end{aligned} \quad (\text{A9})$$

where $K_3 \equiv (\varepsilon_1^r K_2 - \varepsilon_2^r K_1)/(\varepsilon_2^r \varepsilon_1^o - \varepsilon_1^r \varepsilon_2^o)$, and to

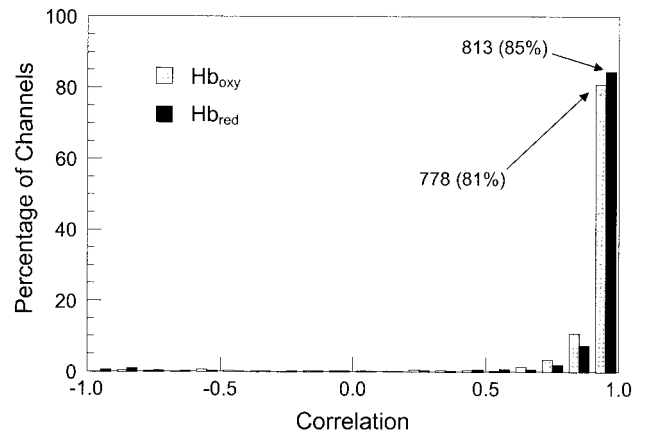


Fig. 14. Histograms of the correlations between Hb concentration change time series derived from reconstructed two-wavelength absorption coefficient images and the corresponding time series estimated from normalized detector data by using a MBL. Gray bars, Hb_{oxy} ; black bars, Hb_{red} .

$$\begin{aligned}
\frac{\varepsilon_1^o[\overline{\mu_{a2}}(t)d_2 - K_2] - \varepsilon_2^o[\overline{\mu_{a1}}(t)d_1 - K_1]}{\varepsilon_1^o\varepsilon_2^r - \varepsilon_2^o\varepsilon_1^r} &= \frac{\varepsilon_2^oK_1 - \varepsilon_1^oK_2}{\varepsilon_1^o\varepsilon_2^r - \varepsilon_2^o\varepsilon_1^r} \\
&+ \frac{\varepsilon_1^o\overline{\mu_{a2}}(t)d_2 - \varepsilon_2^o\overline{\mu_{a1}}(t)d_1}{\varepsilon_1^o\varepsilon_2^r - \varepsilon_2^o\varepsilon_1^r} \\
= K_4 + \frac{\varepsilon_1^o\varepsilon_2^o(d_2 - d_1)}{\varepsilon_1^o\varepsilon_2^r - \varepsilon_2^o\varepsilon_1^r} \bar{c}^o + \frac{\varepsilon_1^o\varepsilon_2^rd_2 - \varepsilon_2^o\varepsilon_1^rd_1}{\varepsilon_1^o\varepsilon_2^r - \varepsilon_2^o\varepsilon_1^r} \bar{c}^r,
\end{aligned} \tag{A10}$$

where $K_4 \equiv (\varepsilon_2^oK_1 - \varepsilon_1^oK_2)/(\varepsilon_1^o\varepsilon_2^r - \varepsilon_2^o\varepsilon_1^r)$. Thus, in conclusion, the quantities plotted in Figs. 10, 12(b), and 13 are linear functions of the true time-varying hemoglobin concentrations \bar{c}^o and \bar{c}^r , provided that $|d_1 - d_2| \ll d_1, d_2$.

The validity of the assumptions underlying the MBL, and of the further assumption at the end of the preceding paragraph, has been subjected to the following test. Taking a set of experimental two-wavelength detector time series as the starting point, we have done the following: first, computed \bar{c}^o and \bar{c}^r time series for each source–detector channel by using Eqs. (A9) and (A10); second, reconstructed the image time series $\mu_{a1}(\mathbf{r}, t)$ and $\mu_{a2}(\mathbf{r}, t)$, using the algorithm of Ref. 9, and from these computed the image time series $c^o(\mathbf{r}, t)$ and $c^r(\mathbf{r}, t)$ by using Eqs. (A7) and (A8); third, computed the predicted $\bar{c}^o(t)$ and $\bar{c}^r(t)$ time series for each source–detector channel from the hemoglobin images produced in the preceding step. Following this, the correlations between every MBL-derived time series and the corresponding image-derived time series were computed. Histograms of the resulting Hb_{oxy} correlations and Hb_{red} correlations are shown in Fig. 14. Of the 961 channels, 778 (81%) had correlations >0.9 for the Hb_{oxy} time series, and 813 (85%) had correlations >0.9 for the Hb_{red} time series. The channels for which the correlations are ≤ 0.5 fall into two categories for which high correlations were not expected: those for which the source–detector separation was at or near its maximal value and those for which the source and detector are collocated.

This research was supported by the National Institutes of Health (NIH) under grants 1R43CA91725-1A1, R21-HL67387, R21-DK63692, and R41-CA96102; by the U.S. Army under grant DAMD017-03-C-0018; by the New York State Department of Health; and by the Susan G. Komen Foundation under grant IMG0403022.

References and Note

1. C. H. Schmitz, H. L. Graber, R. D. Levina, M. B. Levin, and R. L. Barbour, "Data integrity assessment and instrument calibration for the DYNOT imaging system," in *Biomedical Topical Meetings on CD-ROM* (Optical Society of America, Washington, D.C., 2004), presentation ThF28.
2. C. H. Schmitz, M. Löcker, J. M. Lasker, A. H. Hielscher, and R. L. Barbour, "Instrumentation for fast functional optical tomography," *Rev. Sci. Instrum.* **73**, 429–439 (2002).
3. C. H. Schmitz, H. L. Graber, R. L. Levina, M. B. Levin, and R. L. Barbour, "Data integrity assessment and instrument calibration for the DYNOT imaging system," in *Biomedical Topical*

Meetings on CD-ROM (Optical Society of America, Washington, D.C., 2004), presentation WF35.

4. C. H. Schmitz, Y. Pei, H. L. Graber, J. M. Lasker, A. H. Hielscher, and R. L. Barbour, "Instrumentation for real-time dynamic optical tomography," in *Photon Migration, Optical Coherence Tomography, and Microscopy*, S. Andersson-Engels and M. Kaschke, eds., *Proc. SPIE* **4431**, 282–291 (2001).
5. D. P. Klemer, R. L. Barbour, C. H. Schmitz, R. L. Graber, Y. Pei, R. E. Hardin, M. S. Katz, N. A. Franco, and A. G. Smeraldi, "Multi-site near-infrared tomographic imaging of the brain," in *Biomedical Topical Meetings on CD-ROM* (Optical Society of America, Washington, D.C., 2004), presentation WF35.
6. A. G. Smeraldi, N. A. Franco, H. L. Graber, D. P. Klemer, R. E. Hardin, M. S. Katz, C. H. Schmitz, T. F. Panetta, and R. L. Barbour, "Evaluation of peripheral vascular disease using non-invasive dynamic optical tomography," in *Biomedical Topical Meetings on CD-ROM* (Optical Society of America, Washington, D.C., 2004), presentation WF36.
7. R. E. Hardin, D. P. Klemer, M. S. Katz, N. A. Franco, H. L. Graber, C. H. Schmitz, R. L. Barbour, A. G. Smeraldi, and T. F. Panetta, "Application of dynamic optical tomography for the detection of a multi-phase physiologic response to Valsalva maneuver in healthy breast tissue," in *Biomedical Topical Meetings on CD-ROM* (Optical Society of America, Washington, D.C., 2004), presentation WF37.
8. M. S. Katz, R. E. Hardin, N. A. Franco, A. D. Smeraldi, D. P. Klemer, C. H. Schmitz, H. L. Graber, and R. L. Barbour, "Physiological variation in vascular reactivity of breast tissue over the menstrual cycle demonstrated by optical tomography," in *Biomedical Topical Meetings on CD-ROM* (Optical Society of America, Washington, D.C., 2004), presentation WA5.
9. Y. Pei, H. L. Graber, and R. L. Barbour, "Influence of systematic errors in reference states on image quality and on stability of derived information for DC optical imaging," *Appl. Opt.* **40**, 5755–5769 (2001).
10. R. L. Barbour, H. L. Graber, Y. Pei, S. Zhong, and C. H. Schmitz, "Optical tomographic imaging of dynamic features of dense-scattering media," *J. Opt. Soc. Am. A* **18**, 3018–3036 (2001).
11. Y. Pei, H. L. Graber, Y. Xu, and R. L. Barbour, "dynaLYZE—an analysis package for time-series NIRS imaging data," in *Biomedical Topical Meetings on CD-ROM* (Optical Society of America, Washington, D.C., 2004), presentation FH42.
12. R. A. Nishimura and A. J. Tajik, "The Valsalva maneuver and response revisited," *Mayo Clin. Proc.* **61**, 211–217 (1986).
13. R. K. Jain, "Normalizing tumor vasculature with anti-angiogenic therapy: a new paradigm for combination therapy," *Nat. Med.* **7**, 987–989 (2001).
14. H. L. Graber, Y. Pei, R. L. Barbour, D. K. Johnston, Y. Zheng, and J. E. Mayhew, "Signal source separation and localization in the analysis of dynamic near infrared optical tomographic time series," in *Optical Tomography and Spectroscopy of Tissue V*, B. Chance, R. R. Alfano, B. J. Tromberg, M. Tamura, and E. M. Sevick-Muraca, eds. *Proc. SPIE* **4955**, 31–51 (2003).
15. R. L. Barbour, H. L. Graber, C. H. Schmitz, F. Tarantini, G. Khoury, D. J. Naar, T. F. Panetta, T. Lewis, and Y. Pei, "Time-frequency analysis of functional optical mammographic images," in *Optical Tomography and Spectroscopy of Tissue V*, B. Chance, R. R. Alfano, B. J. Tromberg, M. Tamura, and E. M. Sevick-Muraca, *Proc. SPIE* **4955**, 84–95 (2003).
16. R. L. Barbour, H. L. Graber, Y. Pei, C. H. Schmitz, Y. Xu, A. Di Martino, F. X. Castellanos, D. P. Klemer, R. E. Hardin, N. A. Franco, M. S. Katz, M. E. Zenilman, A. G. Smeraldi, and T. F. Panetta, "Functional imaging of the vascular bed by dynamic optical tomography," in *Physiology, Function, and Structure from Medical Images*, A. A. Amini and A. Manduca, eds., *Proc. SPIE* **5369**, 132–149 (2004).
17. M. Cope and D. T. Delpy, "System for long-term measurement

- of cerebral blood and tissue oxygenation on newborn infants by near infra-red transillumination," *Med. Biol. Eng. Comput.* **26**, 289–294 (1988).
18. D. T. Delpy, M. Cope, P. Van der Zee, S. Arridge, S. Wray, and J. Wyatt, "Estimation of optical pathlength through tissue from direct time of flight measurement," *Phys. Med. Biol.* **33**, 1433–1442 (1988).
 19. C. H. Schmitz, H. L. Graber, H. B. Luo, I. Arif, J. Hira, Y. L. Pei, A. Bluestone, S. Zhong, R. Andronica, I. Soller, N. Ramirez, S. L. S. Barbour, and R. L. Barbour, "Instrumentation and calibration protocol for imaging dynamic features in dense-scattering media by optical tomography," *Appl. Opt.* **39**, 6466–6486 (2000).
 20. A. Sassaroli and S. Fantini, "Comment on the modified Beer–Lambert law for scattering media," *Phys. Med. Biol.* **49**, N255–N257 (2004).
 21. An interesting implication of the main result of Ref. 20 is that even if pulsed time-resolved or frequency-domain measurements were made, the value of d still could not be experimentally determined.